RSC Advances

PAPER

View Article Online
View Journal | View Issue

Cite this: *RSC Adv.*, 2021, **11**, 28775

Low content Ru-incorporated Pd nanowires for bifunctional electrocatalysis†

Yongdeog Kweon, Sunguk Noh and Jun Ho Shim *

Received 21st July 2021
Accepted 17th August 2021

DOI: 10.1039/d1ra05577a

rsc.li/rsc-advances

This paper reports the facile synthesis and characterization of carbon supported Pd nanowires with low Ru contents (nRuPd/C). An anti-galvanic replacement reaction involving the reduction of Ru(III) ions by nanoporous Pd nanowires to form nRuPd alloy nanowires was observed. A series of nRuPd/C materials with various Ru/Pd ratios were prepared by the spontaneous deposition of a Ru cluster on a Pd nanowire core using different Ru precursor concentrations ($RuCl_3$ = 0.5, 1.0, 5.0 mM). The successful formation of low content Ru-incorporated Pd nanowires without individual Ru clusters were confirmed using physicochemical characterization. The electrocatalytic activity of the nRuPd/C for the oxygen reduction reaction (ORR) and hydrogen evolution reaction (HER) in alkaline media was measured by RDE polarization experiments. The electrocatalytic activity varied greatly depending on the Ru content on the Pd nanowires. Among the catalysts, the prepared Pd nanowires incorporated with a very small amount of Ru (*ca.* 1.4 wt%) exhibited excellent electrocatalytic activity toward the ORR and HER: positive ORR/HER onset and $E_{1/2}$ potentials, higher *n* value, and lower Tafel slope.

1 Introduction

Fossil fuels, the main source of carbon dioxide emissions, are still being used in large quantities, making it difficult to reduce environmental pollution. Low-cost renewable energy, such as energy conversion reactions to replace fossil fuels, has long been studied, but fundamental and substantial improvements remain a challenge.[1,2] Moreover, the growing demand for renewable energy increases the need to develop alternative energy and storage systems, such as fuel cells,[3–6] water splitting,[7–10] and metal–air batteries.[11–13] As part of these systems, catalysis and catalyst design in half-cell reactions, such as the oxygen reduction reaction (ORR), oxygen evolution reaction (OER), and hydrogen evolution reaction (HER), have attracted considerable attention and include fundamental and applied studies.[14–18] In this regard, efficient and affordable catalysts that can reduce the overpotential and energy consumption are of particular interest.

Over the last two decades, platinum used in the ORR and HER has been considered an industrially state-of-the-art catalyst. In particular, alloying Pt with various metals, including precious metals such as Au, Ru, and Pd, to achieve higher activity at lower potentials and enhanced stability has been a major focus of alternative energy systems.[19–22] For example, Zhong *et al.* reported the first example of ultrathin Pt–Au alloy nanowires featuring composition-tunable and (111) facet-dominant surface properties, and the electrocatalytic enhancement for the ORR.[19] Alloyed PtRu[20] and PtPd[21] catalysts synthesized by the carbon-based catalyst supports have been also considered the most efficient catalysts for HER or ORR. However, they are rarely used as electrocatalysts for bifunctional ORR/HER.

On the other hand, as demand for Pt increases, it is not economical in a long-term perspective owing to its high cost and scarcity. Therefore, extensive research has been conducted to develop highly active and durable electrocatalysts without Pt. Pd materials have been considered alternative catalysts because they have higher methanol tolerance, free from CO poisoning, excellent catalytic activity, and relatively inexpensive.[23–27] Recently, Pd-based bimetallic nanostructures, particularly PdPt,[28–30] PdRu,[31,32] PdNi,[33–35] PdCo,[36–38] and PdAu,[39,40] have been developed widely as promising candidates because of their strain effects and electronic interplay.[41–46]

The authors' group also reported flower-like Pt–Pd nanostructures that exhibited significantly improved ORR activity and stability under acidic conditions.[47] Bimetallic Ir–Pd alloy networks supported on carbon (Ir–Pd/C) nanocomposites exhibited comparable or even better catalytic activity than the benchmarking catalyst, Pd/C (for the ORR) and Ir/C (for the OER).[48] More recently, Ru nanoparticles supported on Pd nanoframes (or *vice versa*) exhibited excellent electrocatalytic HER performance.[49,50] For example, Nanda *et al.* reported the galvanic electroless deposition of Pd-coated Ru nanocrystals supported on an N-doped graphene surface to boost the HER performance and efficient alcohol tolerant ORR.[49] Hong *et al.* proposed the controllable synthesis of mesoporous Pd@Ru core–shell bimetallic nanorods as effective HER catalysts.[50]

Department of Chemistry, Institute of Basic Science, Daegu University, Gyeongsan 38453, Republic of Korea. E-mail: junhoshim@daegu.ac.kr

† Electronic supplementary information (ESI) available. See DOI: 10.1039/d1ra05577a

Indeed, Ru incorporation on another metallic support resulted in exceptional performance and stability toward the ORR. Therefore, Ru-based bimetallic nanostructures have the potential to replace platinum as an alternative ORR catalyst.

This paper reports the synthesis of nanoporous RuPd nanowires supported on carbon (nRuPd/C) through a facile two-step process: (1) formation of nPd nanowires using polyvinylpyrrolidone (PVP) in a neutral aqueous solution; and (2) low content Ru incorporation into nPd nanowires with an anti-galvanic replacement reaction (AGRR). The resulting nRuPd/C nanowires exhibited comparable or even better bifunctional electrocatalytic activity than the benchmarking catalyst (Pt/C) for the ORR and HER.

2 Experimental

2.1. Reagents and characterizations

Palladium(II) chloride ($PdCl_2$) was purchased from Alfa Aesar. Ruthenium(III) chloride hydrate ($RuCl_3 \cdot xH_2O$), polyvinylpyrrolidone (PVP), potassium tetrachloroplatinate(II) (K_2PtCl_4), sodium dihydrogen phosphate ($NaH_2PO_4 \cdot H_2O$), and sodium hydrogen phosphate (Na_2HPO_4) were obtained from Sigma-Aldrich. Potassium hydroxide (KOH), hydrogen peroxide (H_2O_2), and hydrochloric acid (HCl, 35–37%) were acquired from Duksan. Hydrazine (N_2H_4, 80%) was supplied by TCI. The carbon support (Vulcan XC-72) and commercial Pt/C (with a 20 wt% metal loading on Vulcan XC-72) were produced by Premetek. The compositions and morphologies of all synthesized samples were analyzed by high-angle annular dark-field scanning transmission electron microscopy (HAADF-STEM) and transmission electron microscopy (TEM, Hitachi, HF-3300). The structural properties and phases of all samples were determined by powder X-ray diffraction (XRD) using a Diatome MPD for bulk powder. X-ray photoelectron spectroscopy (XPS) was carried out using a ULVAC-PHI Quantera SXM. The Brunauer–Emmett–Teller (BET) surface area and pore size distributions of catalysts were analyzed using a BELSORP-mini II (Mictrotrac-BEL, Japan). All solutions were prepared using purified water (Milli-Q, 18 MΩ cm).

2.2. Synthesis of Pd nanowires

In a typical synthesis, 5.0 mL of 112 mM $PdCl_2$ was added to 20.0 mL of deionized water containing 62.6 mg of PVP and 0.1 mL of HCl in a 100 mL three-necked flask. The reaction solution was maintained at pH = 7.0 with vigorous stirring for 30 min. After complete mixing, hydrazine (2.0 mL of 80 wt%) as a reducing agent was added drop-wise to the mixture, followed by continuously stirring for 12 h. The product was collected by centrifugation, washed several times with water, and dried under vacuum overnight at room temperature.

2.3. Synthesis of Ru-incorporated Pd nanowires

A 10 mg sample of nPd nanowires was dispersed in deionized water (8 mL) by sonication, followed by the addition of 2 mL of a $RuCl_3$ solution (1.0 mM) under stirring. The reaction proceeded for 5 h with stirring. The resulting nRuPd were collected by centrifugation, rinsed with water. The final product was dried overnight at room temperature under a vacuum. Carbon-supported nanoporous PtPd nanowires (nPtPd/C) from Pd nanowires were also prepared in the same manner for comparison.

2.4. Electrochemical measurements

All electrochemical measurements were performed at room temperature. A graphite rod and a saturated calomel electrode (SCE) were used as the counter and reference electrodes, respectively. All potentials were converted to the reversible hydrogen electrode (RHE) scale using the Nernst equation. The glassy carbon (GC) working electrodes were wet-polished using aluminum powder (particle size 0.05 mm) and a microcloth pad (Buehler) and sonicated in distilled water for 5 min to remove the residual aluminum. The ORR measurements were obtained using a BAS (Bioanalytical Systems) rotating disk electrode (RDE) and RDE-2 rotator (BASi). Cyclic voltammetry (CV) was conducted using a CHI 601E (CH Instruments). For the ORR/HER measurements, 20 μL of a catalyst suspension (2 mg mL^{-1}) was placed on the working electrode. The electrochemical data were corrected for the background current (by subtraction), and the RDE measurements were recorded at electrode rotation rates of 400–3600 rpm.

3 Results and discussion

Fig. 1 presents the proposed mechanism of the nanoporous Ru incorporated Pd nanowires (nRuPd) catalyst. In a typical synthesis, the Pd nanowires were obtained by reducing $PdCl_2$ containing PVP at pH = 7.0, followed by the addition of

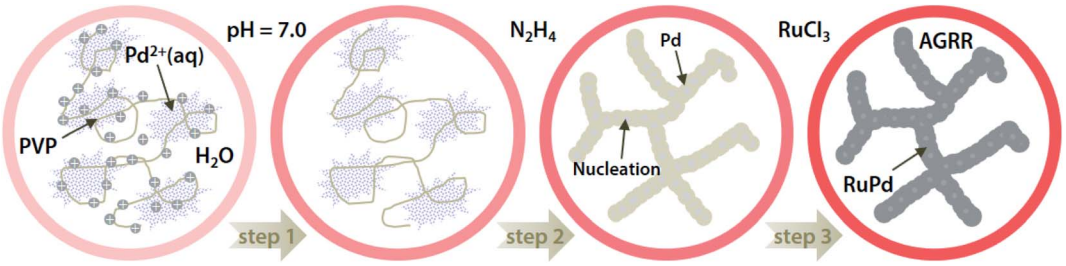

Fig. 1 Schematic diagram of the fabrication process for nRuPd nanowires. Initially, the positively charged PVP led to electrostatic repulsion between the Pd^{2+} ions. Pd nanowires formed networks as the PVP polymer chains were connected to each other at neutral pH (steps 1 and 2). The Ru metal precursor reacted spontaneously with the formed nPd nanowire frames through the AGRR, resulting in nRuPd nanowires (step 3).

hydrazine. Ru(III) was then added to a dispersed nPd nanowire solution and left to stand for 5 h, resulting in the formation of Ru incorporated Pd nanowires. The formation of nPd nanowires was affected by the pH of PVP because the PVP polymer chains connected to each other easily as the polymer was neutral.[51] For nRuPd nanowires, Ru was doped spontaneously on the surface of the Pd nanowires at room temperature, even though the standard reduction potential of Pd^{2+}/Pd ($E^{o} = 0.915$ V *vs.* SHE) is higher than that of Ru^{3+}/Ru ($E^{o} = 0.60$ V *vs.* SHE).[52]

Anode (oxidation):

$$Pd(s) \rightarrow Pd^{2+}(aq) + 2e^{-} \ (E^{o} = +0.915\ V)$$

Cathode (reduction):

$$Ru^{3+}(aq) + 3e^{-} \rightarrow Ru(s) \ (E^{o} = +0.60\ V)$$

Overall:

$$3Pd(s) + 2Ru^{3+}(aq) \rightarrow 3Pd^{2+}(aq) + 2Ru(s)$$

This is opposite to the classic galvanic reaction process, namely anti-galvanic replacement reaction (AGRR). The nRuPd catalyst was composed of Pd nanowires as the basic frame of the network structure decorated with Ru nanoparticles.

Fig. 2 presents typical TEM and STEM mapping images of nPd and nRuPd nanowires. The as-prepared nRuPd exhibited a 3D fiber-like morphology, which is similar to the backbone and grains of the pristine nPd nanowires (Fig. 2a and b). No significant isolated nanocrystals were observed, confirming the high-yield formation of the nPd and nRuPd nanowires. The nRuPd nanostructures were well-dispersed and appeared to have a narrow size distribution (5.9 ± 0.6 nm). Fig. 2c shows a HRTEM image of nRuPd nanowires. The lattice fringes

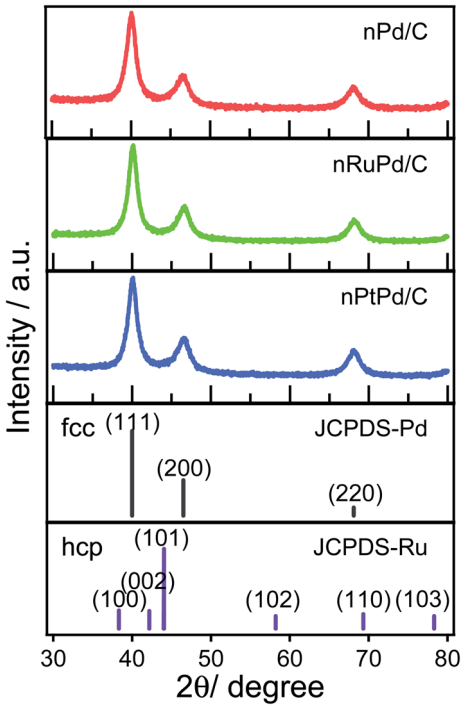

Fig. 3 XRD patterns of nPd/C, nRuPd/C and nPtPd/C catalysts.

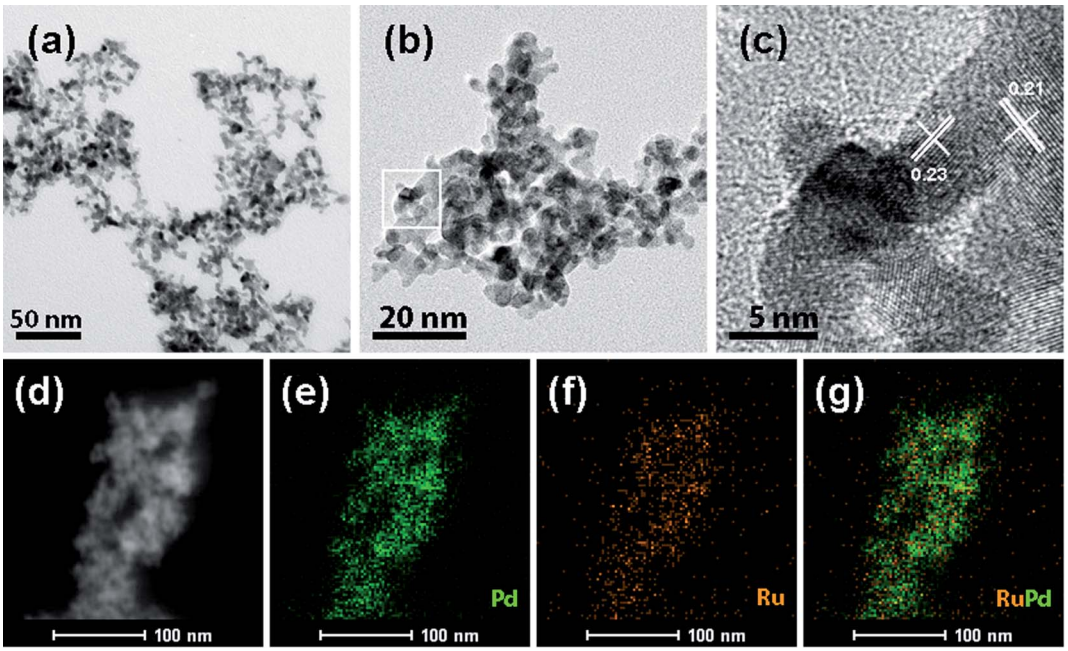

Fig. 2 TEM images of (a) nPd and (b) nRuPd, illustrating the formation of fiber-like nanostructures. (c) Magnified parts of the typical nanochain taken from the boxed areas in (b). (d–g) STEM image of the fiber-like nRuPd nanowires and corresponding EDS elemental maps of Pd, Ru, and RuPd, respectively.

showed an interplanar spacing of 0.23 nm (for Pd only) and 0.21 nm (for nRuPd), corresponding to the lattice spacing of face-centered cubic (fcc) Pd (111) facets. In contrast, the Ru(101) plane showed lattice fringes with an interplanar distance of 0.21 nm. Fig. 2d–g shows HAADF-STEM images and EDS elemental maps of nRuPd. Pd and Ru in nRuPd showed a uniform distribution, indicating that Ru(0) tends to form on the exposed Pd(0) surface rather than form individual Ru(0). Although it was difficult to identify the grain boundaries between Ru and Pd in the prepared nRuPd sample after the AGRR process, EDS mapping detected Ru deposited on the surface of the nPd nanowires in nRuPd (Fig. 2g). The measured atomic ratio (Ru : Pd) of nRuPd nanowires was approximately 1 : 11.8 from EDS (see Fig. S1†). Similar structural behavior was also observed for nPtPd, prepared in the same manner (Fig. S2†).

Fig. 3 shows XRD patterns of the nPd/C, nRuPd/C, and nPtPd/C nanowires. The XRD peaks at 40.06°, 46.55°, and 68.14° 2θ correspond to the (111), (200), and (220) crystal planes of fcc (JCPDS #88-2335) of Pd, respectively. The nPtPd/C catalyst also displayed similar XRD patterns. No noticeable peaks associated with Ru at 38.6°, 42.1°, 44.1°, 58.2°, 69.3°, and 78.3° 2θ, corresponding to (100), (002), (101), (102), (110), and (103) crystal planes, respectively, were observed at nRuPd/C. This is probably due to the low Ru content and the combination of a binary alloy from nRuPd. Moreover, the (111) and (200) lattice peaks for fcc Pd were consistent with those of the XRD patterns of Ru atoms in the absence of hcp Ru signals.[53] On the other hand, the XRD patterns of nRuPd/C showed a slight peak shift at 40.15° 2θ compared to nPd/C or nPtPd/C (Fig. S3†), indicating the binary phase of the nRuPd/C alloy. Considering the atomic radius of Ru (1.34 Å) and Pd (1.37 Å), introducing Ru atoms in the Pd lattice causes a peak shift to higher angles.

XPS was performed to analyze the surface electronic states of nRuPd/C. Fig. 4a shows a wide scan survey spectrum of the nRuPd/C, showing Ru, Pd, and C in the as-prepared sample. Fig. 4b shows the high-resolution spectra of the Pd 3d electrons in the nRuPd/C catalyst. The peaks with binding energies at 339.9 eV and 334.7 eV were assigned to the Pd $3d_{3/2}$ and Pd $3d_{5/2}$ electrons, respectively.[54] The peaks at the lower energies of 334.7 and 340.0 eV were assigned to metallic Pd,[55] while the peaks at higher binding energies of 335.7 and 341.1 eV were ascribed to the Pd (II) species.[54,56] The Ru $3p_{3/2}$ peak was also deconvoluted into two components, which were identified as

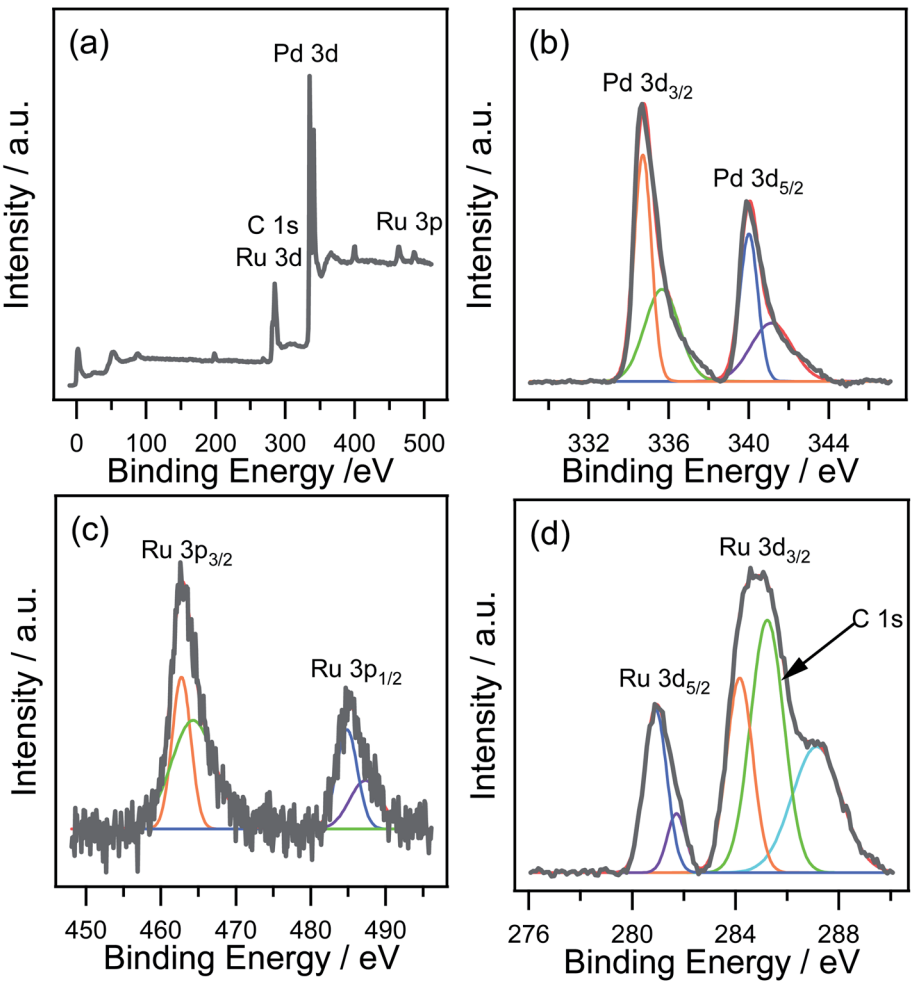

Fig. 4 (a) XPS survey spectra for nRuPd. XPS spectrum of (b) Pd 3d, (c) Ru 3p and (d) Ru 3d.

RuO_2 (462.7 eV) and RuOH (464.3 eV) (Fig. 4c).[57] The peaks at Ru $3d_{5/2}$ (280.9 eV) and Ru $3d_{3/2}$ (284.2 eV) were assigned to metallic Ru. On the other hand, the peaks at 281.7 and 287.1 eV revealed the presence of RuO_2 (Fig. 4d). This was attributed to the oxidation of Ru nanoparticles during sample preparation.[58,59] Ru metal and RuO_2 both give asymmetric Ru 3d peaks shapes, and the C 1s peak of the carbon support and Ru 3d regions strongly overlap.

The ORR and HER catalytic activities of the nPd/C, nRuPd/C, nPtPd/C, and Pt/C were investigated by RDE voltammetry under alkaline conditions. A series of nRuPd/C with different Ru concentration (0.5, 1.0, and 5.0 mM of $RuCl_3$) were examined to

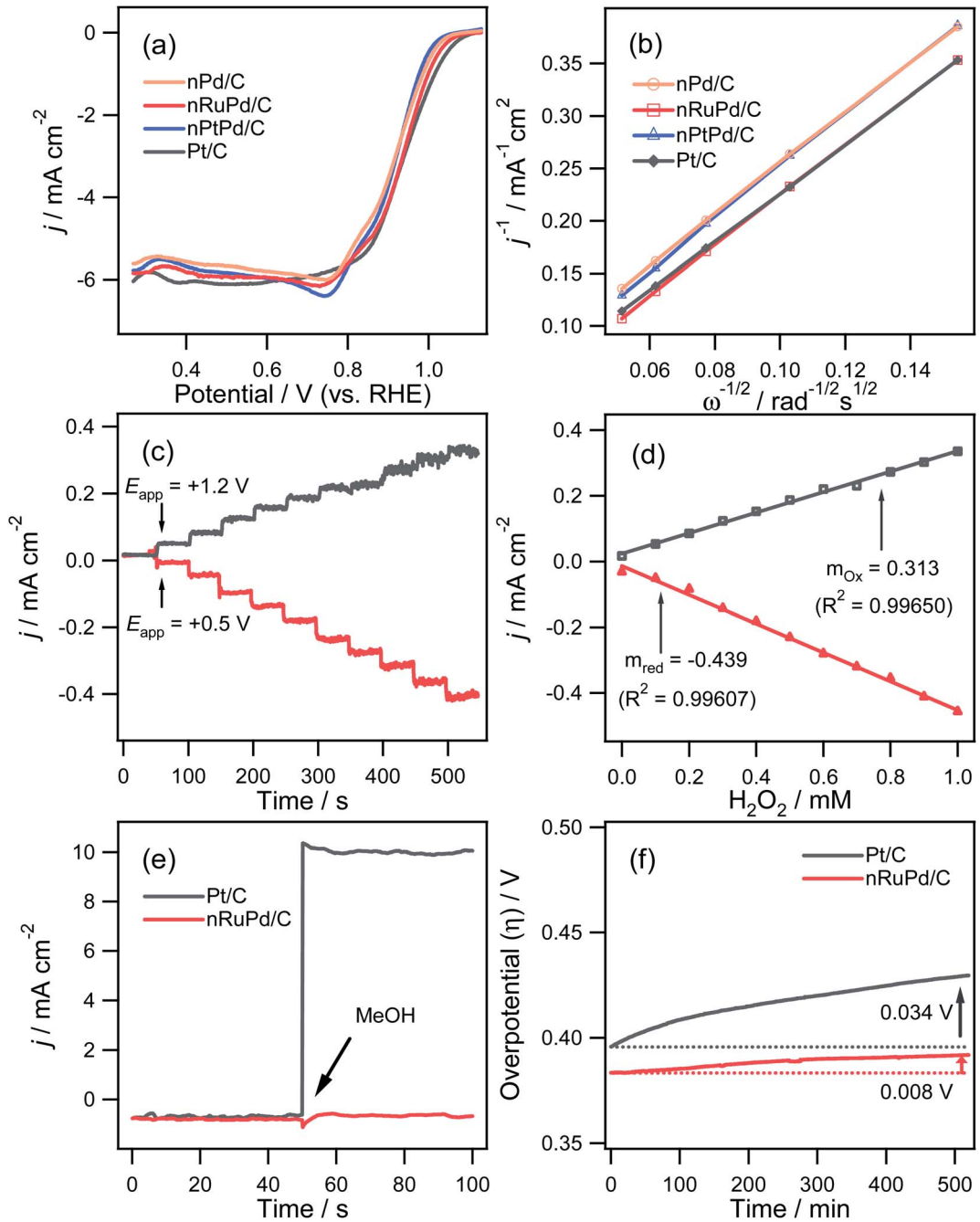

Fig. 5 (a) RDE polarization curves for oxygen reduction in an O_2-saturated 0.1 M KOH solution at a scan rate of 10 mV s^{-1} (rotation speed = 1600 rpm). (b) Koutecky–Levich plots of the ORR corresponding to the RDE voltammetry data at a range of rotation speeds using the current densities measured at 0.41 V *vs.* RHE. (c) Typical amperometric *i*–*t* curves (either at +1.2 V to induce H_2O_2 oxidation or +0.5 V to induce H_2O_2 reduction *vs.* RHE) recorded as a function of time with several successive injections of a H_2O_2 standard solution to vary the concentration in the background solution (deaerated PBS solution at pH 7.4). (d) Corresponding calibration curve. (e) Chronoamperometric responses in an N_2-saturated 0.1 M KOH solution with the addition of 1.0 M methanol at 50 s. (f) Chronopotentiometry stability tests of nRuPd/C and Pt/C catalysts under a current density of −3 mA cm^{-2} in 0.1 M KOH.

Table 1 Electrocatalytic ORR/HER characteristics of the electrocatalysts

	ORR		HER			
Catalysts	$E_{1/2}$ [V]	E_{onset} [V]	n	E [at −10 mA cm^{-2}]	E_{onset} [V]	Tafel slope [mV dec^{-1}]
nPd/C	0.918	1.021	3.76	−0.348	−0.281	251.1
nRuPd/C	0.936	1.038	3.81	−0.011	0.025	50.1
nPtPd/C	0.920	0.999	3.65	−0.202	−0.128	204.9
Pt/C	0.939	1.060	3.92	−0.038	0.011	56.3

explore the effects of Ru incorporation in the nRuPd nanowires on its ORR/HER activity. As shown in Fig. S4a,† the RDE-LSV curves showed that nRu(1.0)Pd/C had the best ORR activity among the catalysts in terms of a positive ORR onset and half-wave potentials ($E_{1/2}$), which are often used as criteria for the catalytic activity. The trend of the HER activity was also similar to that of the ORR performance (Fig. S4b†). Therefore, nRuPd/C and nPtPd were prepared in 1.0 mM of the Ru or Pd precursor.

Fig. 5a presents the ORR polarization curves of nPd/C, nRuPd/C, nPtPd/C, and commercial Pt/C modified GC electrode in O_2-saturated 0.1 M KOH at a scan rate of 10 mV s^{-1} and a rotating rate of 1600 rpm. The resulting $E_{1/2}$ values for nPd/C, nRuPd/C, nPtPd/C, and Pt/C were 0.918, 0.936, 0.920, and 0.939 V, respectively (Table 1). The onset potentials showed a similar trend to that of the ORR $E_{1/2}$ values. Indeed, nRuPd/C showed better ORR activity than nPd/C and nPtPd/C. This suggests that the limited Ru incorporation into nPd nanowires altered the Pd lattice slightly,[53] resulting in enhanced ORR activity over pristine nPd/C. The number of electrons transferred (n) for the ORR was also determined using the Koutecky–

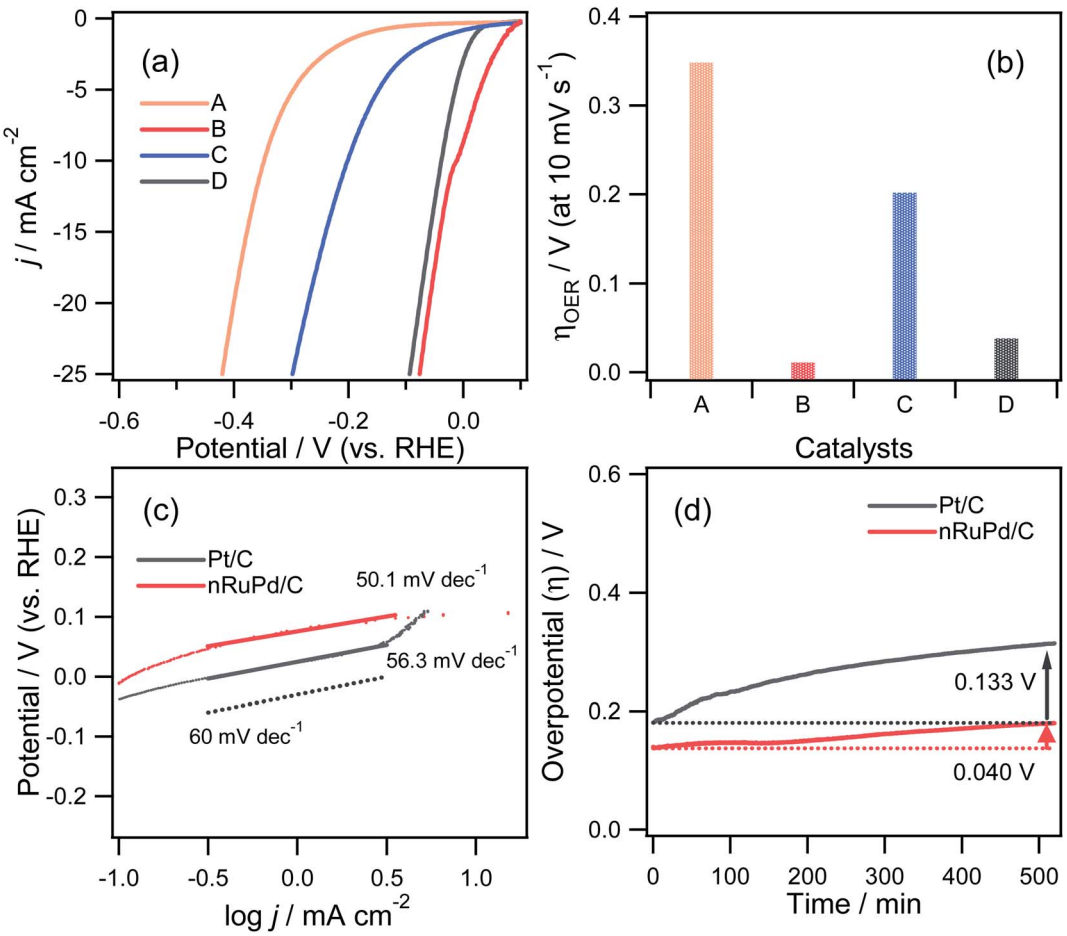

Fig. 6 (a) RDE polarization curves for HER in a N_2-saturated 1.0 M KOH solution at a scan rate of 10 mV s^{-1} (rotation speed = 1600 rpm). (b) Overpotentials (η) at a current density of −10 mA cm^{-2} for each catalyst. (c) Tafel plots for the HER. (d) Chronopotentiometry stability tests of nRuPd/C and Pt/C catalysts under a current density of −10 mA cm^{-2} in 1.0 M KOH. The electrodes used in the electrocatalytic HER: (A) nPd/C, (B) nRuPd/C, (C) nPtPd/C, and (D) Pt/C.

Levich (K–L) equation, as shown in Fig. 5b.[60] The K–L plots at 0.41 V (*vs.* RHE) exhibited good linearity, indicating first-order kinetics with respect to the reactant concentration. The *n* values for nPd/C, nRuPd/C, nPtPd/C, and Pt/C calculated from the slopes in the K–L plots were 3.76, 3.81, 3.65, and 3.92, respectively. Hence, oxygen is reduced *via* a direct 4-electron transfer pathway in all samples in alkaline solutions. Moreover, all samples showed similar *n* values.

The reaction of hydrogen peroxide, known as an intermediate generated by a 2-electron ORR, is an important factor in evaluating the catalytic activity. Fig. 5c and d shows the chronoamperometric *i*–*t* response of H_2O_2 oxidation (+1.2 V *vs.* RHE) and H_2O_2 reduction (+0.5 V *vs.* RHE) using the nRuPd/C catalyst. The results revealed high sensitivity (0.313 mA cm^{-2} mM^{-1} for oxidation and 0.439 mA cm^{-2} mM^{-1} for reduction) and a rapid response time (~2.0 s), low detection limit (~1.5 μM), and reasonable linear dynamic range. These results confirm that the catalytic activity of the ORR is excellent in thermodynamic and kinetic aspects. Moreover, there was no appreciable change in the current density for nRuPd/C after adding MeOH (1.0 M), while a significant increase in current density was observed with Pt/C (Fig. 5e). The nRuPd/C catalyst exhibited a high methanol tolerance compared to Pt/C because the methanol oxidation reaction was suppressed. The ORR durability of the nRuPd/C and Pt/C was confirmed by measuring the steady-state polarization stability using the chronopotentiometric method at −3.0 mA cm^{-2} for the ORR at a rotation speed of 1600 rpm for more than 9 h. A steady decrease in the overpotential ($\Delta\eta$) of 0.92 mV h^{-1} and 3.92 mV h^{-1} was observed for nRuPd/C and Pt/C, respectively, suggesting that nRuPd/C had reasonable ORR stability compared to Pt/C (Fig. 5f).

The catalytic performance of nPd/C, nRuPd/C, nPtPd/C, and Pt/C catalysts toward the HER was also investigated by RDE voltammetry under alkaline conditions. Fig. 6a presents the normalized RDE voltammetry curves recorded in the N_2-saturated 1.0 M KOH solution at 1600 rpm with each catalyst. The nRuPd/C catalyst was superior to the nPd/C, nPtPd/C, and Pt/C catalysts. For example, the overpotential ($\eta = E_o - E$) of nRuPd/C at the benchmark current density of −10 mA cm^{-2} was less negative than that of the other catalysts (Fig. 6b): nPd/C (347.8 mV *vs.* RHE), nRuPd/C (11.7 mV *vs.* RHE), nPtPd/C (201.8 mV *vs.* RHE), and Pt/C (37.8 mV *vs.* RHE). The onset potential for all catalysts showed a similar trend to that of η, suggesting that nRuPd/C caused the rapid HER. As shown in Fig. 6c, a lower Tafel slope of nRuPd/C (50.1 mV dec^{-1}) compared to Pt/C (56.3 mV dec^{-1}) was obtained, highlighting the merits of Ru incorporation into nPd nanowires. Furthermore, nRuPd/C also exhibited superior HER durability, as revealed by the chronopotentiometric responses at −10 mA cm^{-2} for the HER at a rotation speed of 1600 rpm for

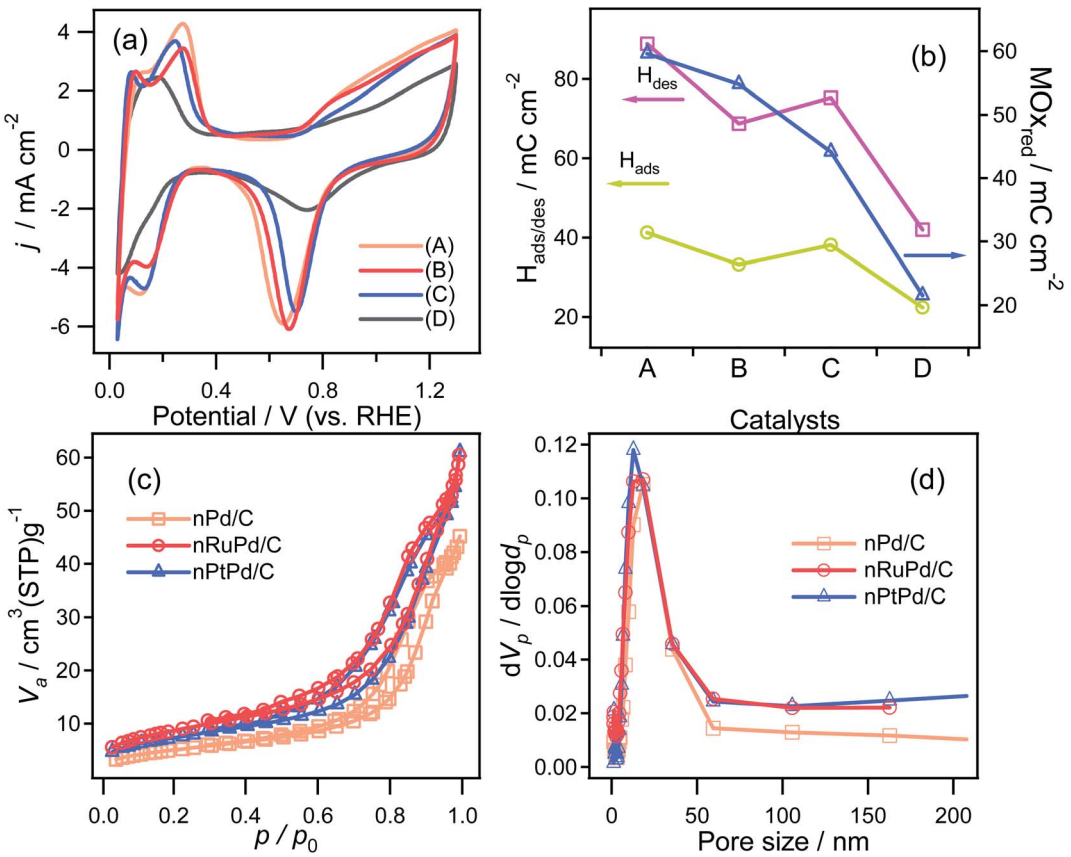

Fig. 7 (a) CV curves recorded in a 0.1 M $HClO_4$ solution deaerated with N_2 purging gas at a scan rate of 20 mV s^{-1}. (b) Plots of the integrated charges of H_{ads} (○), H_{des} (□), and MOx_{red} (Δ). (c) BET surface areas and (d) pore-size distributions of as-prepared electrodes. The electrodes used in the electrocatalytic ORR and HER: (A) nPd/C, (B) nRuPd/C, (C) nPtPd/C, and (D) Pt/C.

more than 9 h. The decay of the $\Delta\eta$ values was 4.6 mV h^{-1} and 15.4 mV h^{-1} for nRuPd/C and for Pt/C, respectively.

Based on the obtained electrocatalytic performance, nRuPd/C provided better ORR and HER activity than the other catalysts in an alkaline medium due to the incorporation of Ru. Table S1† shows a list of several reported Ru-based catalysts with various structural features. On the other hand, the electrochemically active surface area (ECSA) is also an important factor in evaluating the catalytic activity of an electrocatalyst. The electrochemical properties of as-prepared catalysts were investigated by CV in a N_2-saturated 0.1 M $HClO_4$ solution at a scanning rate of 20 mV s^{-1} (Fig. 7a). A cyclic voltammogram obtained with each catalyst showed three distinctive regions: a double-layer capacitive region, hydrogen adsorption/desorption, and a metal oxide formation/reduction region. The anodic peaks at *ca.* 0.71 V (*vs.* RHE) corresponded to the formation of metal surface oxides (MOx_{red}) and the cathodic peak at *ca.* 0.85 V (*vs.* RHE) corresponded to their reduction. Compared to the other electrodes, a significant increase in the MOx_{red} charging current was obtained for nRuPd/C (*ca.* 55 mC cm^{-2}), which was ascribed to the enlarged surface area of the catalysts (Fig. 7b). For comparison, nitrogen adsorption–desorption isotherms were used to obtain the BET surface area and pore size distribution of the prepared catalysts. As shown in Fig. 7c and d, all the isotherms were classified as type IV, and the H3 lag loop appeared at relative pressures (p/p_0) from 0.6 to 1.0, indicating the mesoporous structure of the catalyst. These results suggested the presence of large channel-like pores within a narrow pore size distribution range.[61] Moreover, such pore structures are critical to improving the electrical performance of materials. The mesopores can act as a buffer to store the solution and promote fast mass transport within the porous materials by minimizing diffusion distances.[62,63] The S_{BET}, pore volume, and pore size of the supported nPd catalyst were 17.782 m^2 g^{-1}, 0.069645 cm^3 g^{-1}, and 12.3 nm, respectively, and those of the nRuPd catalyst were 30.341 m^2 g^{-1}, 0.091713 cm^3 g^{-1}, and 9.4 nm, respectively. These values suggest that the addition of Ru increased the specific surface area and pore volume, which likely enhanced the catalytic performance.

4 Conclusions

This paper reported the preparation of a carbon-supported nRuPd catalyst through a facile two-step process using a straightforward synthetic strategy. The nRuPd nanowires produced unique structural features, where the core nPd nanowires were decorated spontaneously by the ultra-low Ru contents. The Ru metal precursor reacted spontaneously with nPd metal nanowires through an AGRR-like mechanism, resulting in a nRuPd/C. The electrochemical tests showed that this nRuPd catalyst exhibited excellent bifunctional ORR/HER catalytic activity with the benchmarking catalyst (Pt/C) for the ORR and HER: positive ORR/HER onset and $E_{1/2}$ potentials, higher n value, and lower Tafel slope. The catalyst also presented superior ORR/HER stability, as revealed by the chronopotentiometric responses at −3.0 mA cm^{-2} for the ORR/HER at a rotation speed of 1600 rpm for more than 9 h. Furthermore, ECSA and BET analysis confirmed that adding Ru to the nPtPd nanowires increased certain surface areas and pore volumes, resulting in improved catalytic ORR/HER performance.

Conflicts of interest

There are no conflicts to declare.

Acknowledgements

This research was supported by the Daegu University, 2018.

References

1 Q. Zhang, E. Uchaker, S. Candelaria and G. Cao, Nanomaterials for Energy Conversion and Storage, *Chem. Soc. Rev.*, 2013, **42**, 3127–3171.
2 M. B. Kale, R. A. Borse, A. G. A. Mohamed and Y. Wang, Electrocatalysts by electrodeposition: Recent advances synthesis methods, and applications in energy conversion, *Adv. Funct. Mater.*, 2021, **31**, 2101313.
3 H. A. Firouzjaie and W. E. Mustain, Catalytic advantages, challenges, and priorities in alkaline membrane fuel cells, *ACS Catal.*, 2020, **10**, 225–234.
4 V. Yarlagadda, M. K. Carpenter, T. E. Moylan, R. S. Kukreja, R. Koestner, W. Gu, L. Thompson and A. Kongkanand, Boosting fuel cell performance with accessible carbon mesopores, *ACS Energy Lett.*, 2018, **3**, 618–621.
5 B. Fang, L. Daniel, A. Bonakdarpour, R. Govindarajan, J. Sharman and D. P. Wilkinson, Dense Pt nanowire electrocatalyst for improved fuel cell performance using a graphitic carbon nitride-decorated hierarchical nanocarbon support, *Small*, 2021, **17**, 2102288.
6 Y.-J. Wang, B. Fang, H. Li, X. T. Bi and H. Wang, Progress in modified carbon support materials for Pt and Pt-alloy cathode catalysts in polymer electrolyte membrane fuel cells, *Prog. Mater. Sci.*, 2016, **82**, 445–498.
7 W. Zhong, Z. Wang, N. Gao, L. Huang, Z. Lin, Y. Liu, F. Meng, J. Deng, S. Jin, Q. Zhang and L. Gu, Coupled vacancy pairs in Ni-doped CoSe for improved electrocatalytic hydrogen production through topochemical deintercalation, *Angew. Chem., Int. Ed.*, 2020, **59**, 22743–22748.
8 W. Zhong, B. Xiao, Z. Lin, Z. Wang, L. Huang, S. Shen, Q. Zhang and L. Gu, $RhSe_2$: A superior 3D electrocatalyst with multiple active facets for hydrogen evolution reaction in both acid and alkaline solutions, *Adv. Mater.*, 2021, **33**, 2007894.
9 S. Shen, Z. Lin, K. Song, Z. Wang, L. Huang, L. Yan, F. Meng, Q. Zhang, L. Gu and W. Zhong, Reversed active sites boost the intrinsic activity of graphene-like cobalt selenide for hydrogen evolution, *Angew. Chem., Int. Ed.*, 2021, **60**, 12360–12365.
10 Z. Lin, B. Xiao, Z. Wang, W. Tao, S. Shen, L. Huang, J. Zhang, F. Meng, Q. Zhang, L. Gu and W. Zhong, Planar-coordination PdSe2 nanosheets as highly active electrocatalyst for hydrogen evolution reaction, *Adv. Funct. Mater.*, 2021, 2102321.

11 Y. Li and J. Lu, Metal–air batteries: will they be the future electrochemical energy storage device of choice?, *ACS Energy Lett.*, 2017, **2**, 1370–1377.
12 J. Fu, J. S. Corsi, Z. Wang, H. Wei and E. Detsi, Integrated Metal–Air Battery and Selective Electrolytic Leaching Cell for the Preparation of Nanoporous Metals, *ACS Appl. Nano Mater.*, 2018, **1**, 4164–4169.
13 Y.-J. Wang, B. Fang, D. Zhang, A. Li, D. P. Wilkinson, A. Ignaszak, L. Zhang and J. Zhang, A review of carbon-composited materials as air-electrode bifunctional electrocatalysts for metal-air batteries, *Electrochem. Energy Rev.*, 2018, **1**, 1–34.
14 Z. W. Seh, J. Kibsgaard, C. F. Dickens, I. Chorkendorff, J. K. Nørskov and T. F. Jaramillo, Combining theory and experiment in electrocatalysis: Insights into materials design, *Science*, 2017, **355**, eaad4998.
15 S. Ghosh and R. N. Basu, Multifunctional nanostructured electrocatalysts for energy conversion and storage: current status and perspectives, *Nanoscale*, 2018, **10**, 11241–11280.
16 C. Li and J.-B. Baek, Recent advances in noble metal (Pt, Ru, and Ir)-based electrocatalysts for efficient hydrogen evolution reaction, *ACS Omega*, 2019, **5**, 31–40.
17 L. Lu, S. Zou and B. Fang, The critical impacts of ligands on heterogeneous nanocatalysis: a review, *ACS Catal.*, 2021, **11**, 6020–6058.
18 S. Yu, S. Song, R. Li and B. Fang, The lightest solid meets the lightest gas: an overview of carbon aerogels and their composites for hydrogen related applications, *Nanoscale*, 2020, **12**, 19536–19556.
19 F. Chang, S. Shan, V. Petkov, Z. Skeete, A. Lu, J. Ravid, J. Wu, J. Luo, G. Yu, Y. Ren and C.-J. Zhong, Composition tunability and (111)-dominant facets of ultrathin platinum-gold alloy nanowires toward enhanced electrocatalysis, *J. Am. Chem. Soc.*, 2016, **138**, 12166–12175.
20 K. Li, Y. Li, Y. Wang, J. Ge, C. Liu and W. Xing, Enhanced electrocatalytic performance for the hydrogen evolution reaction through surface enrichment of platinum nanoclusters alloying with ruthenium in situ embedded in carbon, *Energy Environ. Sci.*, 2018, **11**, 1232–1239.
21 M. H. Shao, T. Huang, P. Liu, J. Zhang, K. Sasaki, M. B. Vukmirovic and R. R. Adzic, Palladium monolayer and palladium alloy electrocatalysts for oxygen reduction, *Langmuir*, 2006, **22**, 10409–10415.
22 S.-Y. Bae, J. Mahmood, I.-Y. Jeon and J.-B. Baek, Recent advances in ruthenium-based electrocatalysts for the hydrogen evolution reaction, *Nanoscale Horiz.*, 2020, **5**, 43–56.
23 L. Zhang, Q. Chang, H. Chen and M. Shao, Recent advances in palladium-based electrocatalysts for fuel cell reactions and hydrogen evolution reaction, *Nano Energy*, 2016, **29**, 198–219.
24 G. Behmenyar and A. N. Akın, Investigation of carbon supported Pd–Cu nanoparticles as anode catalysts for direct borohydride fuel cell, *J. Power Sources*, 2014, **249**, 239–246.
25 T. Li, Z. Tang, K. Wang, W. Wu, S. Chen and C. Wang, Palladium nanoparticles grown on β-Mo_2C nanotubes as dual functional electrocatalysts for both oxygen reduction reaction and hydrogen evolution reaction, *Int. J. Hydrogen Energy*, 2018, **43**, 4932–4941.
26 A. Chen and C. Ostrom, Palladium-based nanomaterials: synthesis and electrochemical applications, *Chem. Rev.*, 2015, **115**, 11999–12044.
27 H. Begum, M. S. Ahmed, S. Cho and S. Jeon, Freestanding palladium nanonetworks electrocatalyst for oxygen reduction reaction in fuel cells, *Int. J. Hydrogen Energy*, 2018, **43**, 229–238.
28 B. A. Kakade, H. Wang, T. Tamaki, H. Ohashi and T. Yamaguchi, Enhanced oxygen reduction reaction by bimetallic CoPt and PdPt nanocrystals, *RSC Adv.*, 2013, **3**, 10487–10496.
29 Y. Liu, S. Liu, Z. Che, S. Zhao, X. Sheng, M. Han and J. Bao, Concave octahedral Pd@ PdPt electrocatalysts integrating core–shell, alloy and concave structures for high-efficiency oxygen reduction and hydrogen evolution reactions, *J. Mater. Chem. A*, 2016, **4**, 16690–16697.
30 Z. Zhu, Y. Zhai, C. Zhu, Z. Wang and S. Dong, Bimetallic alloy nanowires and nanosponges: A comparative study of peroxidase mimetics and as enhanced catalysts for oxygen reduction reaction, *Electrochem. Commun.*, 2013, **36**, 22–25.
31 K. Kwon, S.-A. Jin, D.-H. Yeon, J. O. Park, D. J. You, J. Cho, H. C. Ham and C. Pak, Synergistic enhancement of activity towards hydrogen oxidation reaction by Palladium–Ruthenium bimetallic catalysts in acidic media, *J. Alloys Compd.*, 2020, **849**, 156642.
32 Z. Wang, C. Li, K. Deng, Y. Xu, H. Xue, X. Li, L. Wang and H. Wang, Ambient nitrogen reduction to ammonia electrocatalyzed by bimetallic PdRu porous nanostructures, *ACS Sustainable Chem. Eng.*, 2018, **7**, 2400–2405.
33 M. Martins, Ö. Metin, B. Šljukić, M. Sevim, C. Sequeira and D. Santos, PdNi alloy nanoparticles assembled on cobalt ferrite-carbon black composite as a fuel cell catalyst, *Int. J. Hydrogen Energy*, 2019, **44**, 14193–14200.
34 M. Maize, H. A. El-Boraey, M. I. Ayad, J. D. Holmes and G. Collins, Controlled morphology and dimensionality evolution of NiPd bimetallic nanostructures, *J. Colloid Interface Sci.*, 2021, **585**, 480–489.
35 H. Liu, C. Koenigsmann, R. R. Adzic and S. S. Wong, Probing ultrathin one-dimensional Pd–Ni nanostructures as oxygen reduction reaction catalysts, *ACS Catal.*, 2014, **4**, 2544–2555.
36 D. N. Son, O. K. Le, V. Chihaia and K. Takahashi, Effects of Co content in Pd-skin/PdCo alloys for oxygen reduction reaction: density functional theory predictions, *J. Phys. Chem. C*, 2015, **119**, 24364–24372.
37 F. Pires and H. Villullas, Pd-based catalysts: Influence of the second metal on their stability and oxygen reduction activity, *Int. J. Hydrogen Energy*, 2012, **37**, 17052–17059.
38 K.-P. Lee, S.-H. Lee, K. S. Sundaram and G. A. Iyengar, Preparation of Co/Pd alloy particles dispersed multiwalled carbon nanotube supported nanocatalysts via gamma irradiation, *Radiat. Phys. Chem.*, 2012, **81**, 1422–1425.
39 W. Jiao, C. Chen, W. You, X. Zhao, J. Zhang, Y. Feng, P. Wang and R. Che, Hollow palladium-gold nanochains with periodic concave structures as superior ORR

electrocatalysts and highly efficient SERS substrates, *Adv. Energy Mater.*, 2020, **10**, 1904072.

40 F. A. Al-Odail, A. Anastasopoulos and B. E. Hayden, The hydrogen evolution reaction and hydrogen oxidation reaction on thin film PdAu alloy surfaces, *Phys. Chem. Chem. Phys.*, 2010, **12**, 11398–11406.

41 T. Chao, X. Luo, W. Chen, B. Jiang, J. Ge, Y. Lin, G. Wu, X. Wang, Y. Hu and Z. Zhuang, Atomically Dispersed Copper-Platinum Dual Sites Alloyed with Palladium Nanorings Catalyze the Hydrogen Evolution Reaction, *Angew. Chem.*, 2017, **129**, 16263–16267.

42 S. Rasul, D. H. Anjum, A. Jedidi, Y. Minenkov, L. Cavallo and K. Takanabe, A Highly Selective Copper-Indium Bimetallic Electrocatalyst for the Electrochemical Reduction of Aqueous CO_2 to CO, *Angew. Chem.*, 2015, **127**, 2174–2178.

43 Q. Lu, G. S. Hutchings, W. Yu, Y. Zhou, R. V. Forest, R. Tao, J. Rosen, B. T. Yonemoto, Z. Cao and H. Zheng, Highly Porous Non-precious Bimetallic Electrocatalysts for Efficient Hydrogen Evolution, *Nat. Commun.*, 2015, **6**, 1–8.

44 J. Ge, P. Wei, G. Wu, Y. Liu, T. Yuan, Z. Li, Y. Qu, Y. Wu, H. Li and Z. Zhuang, Ultrathin Palladium Nanomesh for Electrocatalysis, *Angew. Chem.*, 2018, **130**, 3493–3496.

45 S. Li, Y. Wang, S. Peng, L. Zhang, A. M. Al-Enizi, H. Zhang, X. Sun and G. Zheng, Co-Ni-Based Nanotubes/Nanosheets as Efficient Water Splitting Electrocatalysts, *Adv. Energy Mater.*, 2016, **6**, 1501661.

46 A. Abdelhafiz, A. Vitale, C. Joiner, E. Vogel and F. M. Alamgir, Layer-by-layer Evolution of Structure, Strain, and Activity for the Oxygen Evolution Reaction in Graphene-templated Pt Monolayers, *ACS Appl. Mater. Interfaces*, 2015, **7**, 6180–6188.

47 A. T. N. Nguyen and J. H. Shim, Seedless, one-step synthesis of porous Pt-Pd nanoflowers for electroreduction of oxygen in acidic medium, *Appl. Surf. Sci.*, 2018, **458**, 910–916.

48 A. T. N. Nguyen and J. H. Shim, Facile one-step synthesis of Ir-Pd bimetallic alloy networks as efficient bifunctional catalysts for oxygen reduction and oxygen evolution reactions, *J. Electroanal. Chem.*, 2018, **827**, 120–127.

49 B. K. Barman, B. Sarkar and K. K. Nanda, Pd-coated Ru nanocrystals supported on N-doped graphene as HER and ORR electrocatalysts, *Chem. Commun.*, 2019, **55**, 13928–13931.

50 Y. Luo, X. Luo, G. Wu, Z. Li, G. Wang, B. Jiang, Y. Hu, T. Chao, H. Ju and J. Zhu, Mesoporous Pd@ Ru Core–Shell Nanorods for Hydrogen Evolution Reaction in Alkaline Solution, *ACS Appl. Mater. Interfaces*, 2018, **10**, 34147–34152.

51 F. Lan, D. Wang, S. Lu, J. Zhang, D. Liang, S. Peng, Y. Liu and Y. Xiang, Ultra-low loading Pt decorated coral-like Pd nanochain networks with enhanced activity and stability towards formic acid electrooxidation, *J. Mater. Chem. A*, 2013, **1**, 1548–1552.

52 S. G. Bratsch, Standard electrode potentials and temperature coefficients in water at 298.15 K, *J. Phys. Chem. Ref. Data*, 1989, **18**, 1–21.

53 Y. Sun, Y.-C. Hsieh, L.-C. Chang, P.-W. Wu and J.-F. Lee, Synthesis of Pd_9Ru@Pt nanoparticles for oxygen reduction reaction in acidic electrolytes, *J. Power Sources*, 2015, **277**, 116–123.

54 J. Zhang, A. Feng, J. Bai, Z. Tan, W. Shao, Y. Yang, W. Hong and Z. Xiao, One-pot synthesis of hierarchical flower-like Pd-Cu alloy support on graphene towards ethanol oxidation, *Nanoscale Res. Lett.*, 2017, **12**, 1–8.

55 W. Yan, Z. Tang, L. Li, L. Wang, H. Yang, Q. Wang, W. Wu and S. Chen, Ultrasmall palladium nanoclusters encapsulated in porous carbon nanosheets for oxygen electroreduction in alkaline media, *ChemElectroChem*, 2017, **4**, 1349–1355.

56 J. Tian, W. Wu, Z. Tang, Y. Wu, R. Burns, B. Tichnell, Z. Liu and S. Chen, Oxygen reduction reaction and hydrogen evolution reaction catalyzed by Pd–Ru nanoparticles encapsulated in porous carbon nanosheets, *Catalysts*, 2018, **8**, 329.

57 W. Wang, S. Guo, I. Lee, K. Ahmed, J. Zhong, Z. Favors, F. Zaera, M. Ozkan and C. S. Ozkan, Hydrous ruthenium oxide nanoparticles anchored to graphene and carbon nanotube hybrid foam for supercapacitors, *Sci. Rep.*, 2014, **4**, 1–9.

58 H.-B. Dai, X.-D. Kang and P. Wang, Ruthenium nanoparticles immobilized in montmorillonite used as catalyst for methanolysis of ammonia borane, *Int. J. Hydrogen Energy*, 2010, **35**, 10317–10323.

59 S. Miao, Z. Liu, B. Han, J. Huang, Z. Sun, J. Zhang and T. Jiang, Ru nanoparticles immobilized on montmorillonite by ionic liquids: a highly efficient heterogeneous catalyst for the hydrogenation of benzene, *Angew. Chem.*, 2006, **118**, 272–275.

60 S. Jo, S. Noh, K. R. Wee and J. H. Shim, Structural features of porous CoFe nanocubes and their performance for oxygen-involving energy electrocatalysis, *ChemElectroChem*, 2020, **7**, 3725–3732.

61 M. Thommes, K. Kaneko, A. V. Neimark, J. P. Olivier, F. Rodriguez-Reinoso, J. Rouquerol and K. S. Sing, Physisorption of gases, with special reference to the evaluation of surface area and pore size distribution (IUPAC Technical Report), *Pure Appl. Chem.*, 2015, **87**, 1051–1069.

62 H. A. Hamouda, S. Cui, X. Dai, L. Xiao, X. Xie, H. Peng and G. Ma, Synthesis of porous carbon material based on biomass derived from hibiscus sabdariffa fruits as active electrodes for high-performance symmetric supercapacitors, *RSC Adv.*, 2021, **11**, 354–363.

63 Y. Xing, B. Fang, A. Bonakdarpour, S. Zhang and D. P. Wilkinson, Facile fabrication of mesoporous carbon nanofibers with unique hierarchical nanoarchitecture for electrochemical hydrogen storage, *Int. J. Hydrogen Energy*, 2014, **39**, 7859–7867.